

The Transverse Proximity Effect: A Probe to the Environment, Anisotropy, and Megayear Variability of QSOs.

Michael Schirber¹, Jordi Miralda-Escudé², Patrick McDonald³

¹ *Department of Physics, The Ohio State University, 174 W. 18th Ave, Columbus, OH 43210-1173; schirber@campbell.mps.ohio-state.edu*

² *Department of Astronomy, The Ohio State University, 140 W. 18th Ave, Columbus, OH 43210-1006; jordi@astronomy.ohio-state.edu*

³ *Department of Physics, Jadwin Hall, Princeton University, Princeton, NJ 08544; pm@princeton.edu*

ABSTRACT

The transverse proximity effect is the expected decrease in the strength of the Ly α forest absorption in a QSO spectrum when another QSO lying close to the line of sight enhances the photoionization rate above that due to the average cosmic ionizing background. We select three QSOs from the Early Data Release of the Sloan Digital Sky Survey that have nearby foreground QSOs, with proper line of sight tangential separations of 0.50, 0.82, and 1.10 h^{-1} Mpc. We estimate that the ionizing flux from the foreground QSO should increase the photoionization rate by a factor (94, 13, 13) in these three cases, which would be clearly detectable in the first QSO and marginally so in the other two. We do not detect the transverse proximity effect. Three possible explanations are provided: an increase of the gas density in the vicinity of QSOs, time variability, and anisotropy of the QSO emission. We find that the increase of gas density near QSOs can be important if they are located in the most massive halos present at high redshift, but is not enough to fully explain the absence of the transverse proximity effect. Anisotropy requires an unrealistically small opening angle of the QSO emission. Variability demands that the luminosity of the QSO with the largest predicted effect was much lower 10^6 years ago, whereas the transverse proximity effect observed in the HeII Ly α absorption in QSO 0302-003 by Jakobsen et al. (2003) implies a lifetime longer than 10^7 years. A combination of all three effects may better explain the lack of Ly α absorption reduction. A larger sample of QSO pairs may be used to diagnose the environment, anisotropy and lifetime distribution of QSOs.

1. Introduction

The Ly α forest observed in the spectra of QSOs is the principal tool to study the evolution of the intergalactic medium. Our present understanding of the Ly α forest is based on the assumption that the intergalactic medium is photoionized, and that the absorption features arise from variations in gas density determined by the gravitational evolution of primordial fluctuations. Numerical realizations of Cold Dark Matter models that are supported by independent observational evidence from the Cosmic Microwave Background, galaxy clustering, and weak lensing make predictions for properties such as the distribution of the transmitted flux, the power spectrum, and the transverse sizes of the absorbers that are in broad agreement with observations (e.g., Rauch 1998; Crofts & Fang 1998; McDonald et al. 2000; Croft et al. 2002; Tegmark & Zaldarriaga 2002).

A fundamental quantity for the Ly α forest is the intensity of the ionizing background as a function of redshift, which determines the degree of ionization of the intergalactic medium. One method for measuring this intensity is the proximity effect, which consists of a decline in the strength of the Ly α absorption as the redshift of the QSO is approached, compared to the strength observed at the same redshift in other lines of sight of QSOs with a higher emission redshift. The effect can be interpreted as due to the additional ionization caused by the QSO in its vicinity; the total ionizing radiation is increased near the QSO, reducing the neutral fraction in the absorption systems and decreasing their column density (Carswell et al. 1982; Murdoch et al. 1986; Bajtlik, Duncan, & Ostriker 1988; Scott et al. 2000). Therefore, the effect can be used to measure the background intensity: the more intense the background is, the smaller the proximity effect we expect at a fixed distance from the QSO, because the QSO flux (known from its luminosity) is less important compared to the mean background. The most recent measurement by Scott et al. (2000) yields a value of the photoionization rate of $1.9 \times 10^{-12} \text{ s}^{-1}$, with an error of about 50%, over the redshift range $1.7 < z < 3.8$.

This interpretation of the proximity effect to measure the ionizing background intensity is, however, subject to several systematic uncertainties: (a) Systematic errors in the redshift of the QSO estimated from its emission lines may change the distances inferred from the absorption systems to the QSO. Scott et al. show that the redshifts inferred from the O III and Mg II emission lines are higher by 400 km s^{-1} than the redshift obtained from the Ly α emission line, resulting in a factor of 2 decrease in the inferred background intensity. (b) QSOs could be variable on the photoionization timescale of $\sim 10^4$ years, and the proximity effect reflects the QSO luminosity averaged over a photoionization timescale, which would be systematically lower than the present luminosity because QSOs in a flux-limited sample should be preferentially selected in their bright phase. (c) Some QSOs may be gravitationally lensed, again making them appear on average more luminous than they really are in a flux-limited sample. (d) QSOs are likely associated with dense regions in the universe, and the higher gas density in their vicinity may partially compensate for the decrease in the neutral fraction due to their ionizing flux.

In fact, in the context of the Ly α forest theory based on primordial fluctuations, the value of the

ionizing background intensity can be determined from the observed transmitted flux distribution, once the mean baryon density, gas temperature and power spectrum amplitude are known, because numerical simulations allow one to predict the density and temperature distribution of the gas in the Ly α forest. This method yields a value of the ionizing background intensity that is lower than that found from the proximity effect by a factor of 2 to 3 (e.g., McDonald & Miralda-Escudé 2001; Schirber & Bullock 2003).

Several authors have searched for the transverse proximity effect in the past, starting with Crofts (1989), who observed a triplet of QSOs at $z \sim 2.5$ with separations of 2 to 3 arc minutes, corresponding to time-delays of a few $\times 10^6$ years. No convincing evidence was found for the proximity effect in this and later observations (Møller & Kjærgaard 1992; Fernández-Soto et al. 1995; Liske & Williger 2001). One exception is the case of Q0302-003, where a void of absorption lines was found by Dobrzycki & Bechtold (1991) in the vicinity of a QSO; however, the center of the void is offset by $\Delta z \approx 0.05$ to the blue of the QSO, which corresponds to a surprisingly large separation of $\sim 8h^{-1}$ proper Mpc. These analyses, with detections and otherwise, have been based on taking some measure of the absorption in the region where the proximity effect is expected, and comparing this to an empirical model of absorption systems derived from other QSO line of sights. Most often the absorption has been characterized by the number of Ly α lines with fitted Voigt profiles that are found per unit redshift. A different approach was used by Møller & Kjærgaard and Liske & Williger: they measured the mean transmitted flux distribution in the proximity effect region and compared it to a modeled transmitted flux distribution, derived by assuming that the Ly α forest consists of uncorrelated absorption lines with a distribution of column densities and Doppler parameters obtained from fits to the observed spectra. In this paper, we use the full transmitted flux distribution as a probe to the transverse proximity effect, comparing it instead to the expected distribution obtained from artificial absorption spectra generated from cosmological simulations of the Ly α forest.

This paper presents an analysis of three QSO pairs found in the Sloan Digital Sky Survey Early Data Release, which are close enough for the expected transverse proximity effect to be important. The sample selection and continuum fitting of the spectra is described in §2. The method we use to estimate the probability of observing a certain value of the transmitted flux in the spectrum, with the use of Ly α forest simulations, is described in §3. By comparing the actual spectra to simulated lines of sight, we show in §4 that there is no evidence for the transverse proximity effect in our three pairs. We then model the possible effect of a density enhancement in the vicinity of the QSOs (§5), and discuss the effects of anisotropy (§6) and QSO variability (§7). We assume the flat cosmological model with present matter density $\Omega_m = 0.4$ and Hubble constant $H_0 = 65 \text{ km s}^{-1} \text{ Mpc}^{-1}$ throughout the paper.

Pair	Background QSO	Foreground QSO	z_b	z_f	θ	R_\perp	\mathbf{f}_\perp
1	110819.15 – 005823.9	110813.85 – 005944.5	4.595	4.032	1.89	0.50	14.3
2	134755.67 + 003935.0	134808.79 + 003723.2	3.817	3.620	3.95	1.10	2.29
3	233132.84 + 010620.8	233139.76 + 010427.0	2.639	2.245	2.57	0.82	4.48

Table 1 – The pairs in our sample. *Columns 2 and 3*: Sloan names for background and foreground QSOs. *Columns 4 and 5*: redshifts for both QSOs. *Column 6*: the angular separation between the pairs in arc minutes. *Column 7*: impact parameter in (proper) $h^{-1}\text{Mpc}$. *Column 8*: the Lyman limit flux density in units of $4\pi \times 10^{-21}\text{erg/s/cm}^2/\text{Hz}$ at a distance of R_\perp from the foreground QSO. In terms of the notation in §2.2, this is equal to $\mathbf{f}_f(\nu_H, z_f)$. Note that $\mathbf{f}_\perp = 1$ corresponds to an ionizing background intensity of $J = 10^{-21}\text{erg/s/cm}^2/\text{Hz/sr}$.

2. Sample

The SDSS Early Data Release contains a total of 3814 QSOs with redshifts between 0.15 and 5.03, and magnitudes $15.16 < i^* < 20.82$ (Schneider et al. 2002). We first took from these the 482 QSOs with $z > 2.2$, on which the $\text{Ly}\alpha$ forest spectrum is (at least partly) in the observed wavelength range. For each QSO we searched for the closest neighbor in angular separation, and selected those pairs for which the foreground and background QSO redshifts, z_f and z_b , satisfied $1 + z_f > (1026/1216) \cdot (1 + z_b)$, to ensure that the proximity effect region would not be contaminated by $\text{Ly}\beta$ lines.

Of the pairs that fulfilled this criterion, we selected the three with the largest ratio of the ionizing rate from the foreground QSO, Γ_f , to that of the background ionizing rate, Γ_{bkg} , evaluated on the line of sight of the background QSO at a redshift z_f . The calculation of these ionizing rates is described below (§2.1). We list these 3 pairs in Table 1, along with their redshifts and angular separations, from which we obtained their impact parameter (i.e., the shortest distance between the foreground QSO and the background QSO line of sight). For this distance, we also determined the expected continuum flux from the foreground QSO at the Lyman limit (see §2.1).

2.1. Continuum fitting

To measure the fraction of transmitted flux from the observed QSO spectral flux, one needs to first estimate the continuum flux that would have been observed in the absence of any $\text{Ly}\alpha$ absorption. Here, we use a method similar to the one proposed by Press, Rybicki, & Schneider (1993), based on extrapolating the flux observed at wavelengths longer than $\text{Ly}\alpha$ to the shorter wavelengths where the $\text{Ly}\alpha$ forest absorption is present. The other method that is often used is to assume that the spectral regions between absorption lines are practically free of absorption and can be used to trace the continuum (e.g., Rauch et al. 1997), but this becomes more problematic at high redshift where absorption becomes ubiquitous.

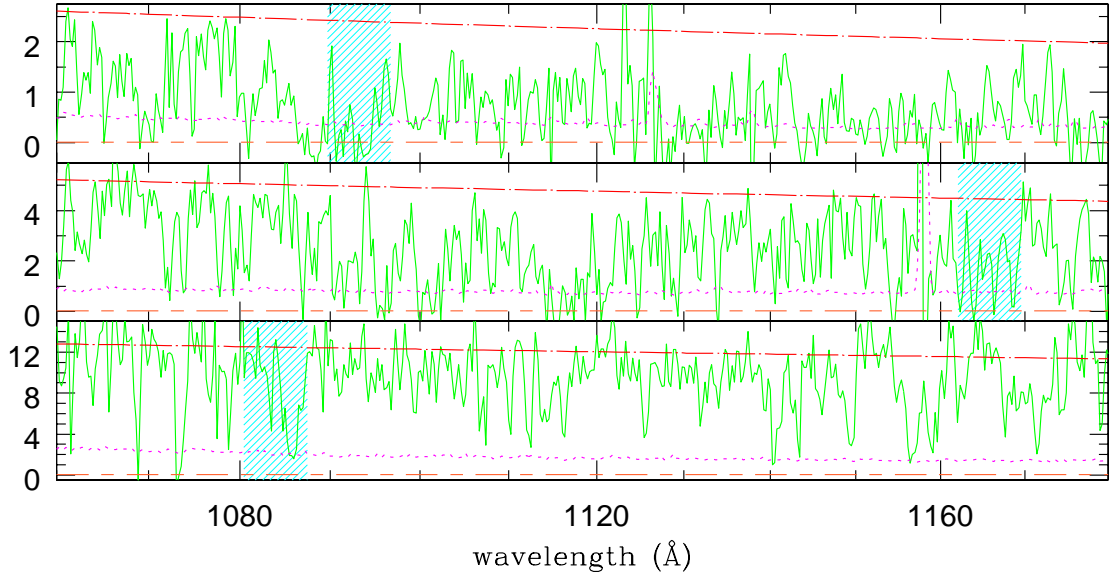


Fig. 1.— *Solid lines*: spectra of background QSOs (in units of 10^{-17} erg/s/cm²/Å) versus rest-frame wavelength. *Top panel* is pair 1, *middle* is pair 2, *bottom* is pair 3. *Dot-dash line*: continuum fit; *dotted line*: noise. Shaded regions are centered at the foreground QSOs redshifts, with rest-frame widths $\Delta v = 2000$ km/s.

We fitted the continuum of each one of the six QSO spectra in the three pairs, using only the wavelength range from the rest-frame Ly α to the observer frame wavelength limit of 8500Å and eliminating the wavelength intervals corresponding to the strong emission lines (Ly α , O I, Si IV-O IV, C IV, C III, Fe III, Fe II) that are given in Table 2 of Vanden Berk et al. (2001). The remaining part of each spectrum was fit with a single power-law, $f_{\lambda} \propto \lambda^{-\alpha_{\lambda}}$. We provide the spectral slope and the fitted continuum flux per unit wavelength at rest-frame 1460 Å in Table 2 for the background QSOs, and in Table 3 for the foreground QSOs. We plot our fits to the background spectra, extrapolated to wavelengths shorter than Ly α , in Figure 1. The observed flux is divided by our continuum to obtain the fraction of transmitted flux, F . The average transmitted flux, \bar{F} , over the Ly α forest region covering the QSO rest-frame wavelength range from 1060 Å to 1180 Å (to avoid the emission lines at Ly α and Ly β) is given in Table 2. We also give the mean transmitted flux measured by Bernardi et al. (2003) over this same region. In terms of $\tau_{eff} \equiv -\ln(\bar{F})$, they measured:¹

$$\tau_{eff} = 2.4 \times 10^{-3} (1+z)^{3.79 \pm 0.18} \quad (1)$$

Our values of the average transmission are similar to those of Bernardi et al. (2003). We will also use the Bernardi et al. (2003) result later in §3 to normalize the optical depth in the numerical

¹Bernardi et al. (2003) also include a small dip in the effective optical depth at $z \sim 3$ that they attribute to helium reionization. We have not included this in our analysis.

Pair	Background spectrum	$\mathbf{f}_b(1460, 0)$	α_λ	\bar{F}_{obs}	\bar{F}_{exp}
1	spSpec-51900-0278-215	1.13	2.62 ± 0.33	0.31	0.30
2	spSpec-51666-0300-414	3.06	1.66 ± 0.07	0.53	0.51
3	spSpec-51821-0384-334	8.90	1.13 ± 0.02	0.80	0.79

Table 2 – *Column 2*: background QSO spectrum name. *Column 3*: flux density at rest-frame 1460 Å in $10^{-17}\text{erg/s/cm}^2/\text{Å}$ for our continuum fit (errors $\leq 2\%$). *Column 4*: spectral slope (with error). *Column 5*: transmitted flux averaged over 1060 – 1180 Å. *Column 6*: mean transmitted flux from Bernardi et al. (2003) averaged over the same wavelengths (see eq. 1).

simulations of the Ly α forest.

2.2. The Ionizing Flux from the Foreground QSO

The signature of the proximity effect is an increase in transmitted flux in the background QSO spectrum. Photoionization equilibrium of the hydrogen in the IGM (neglecting collisional ionization) implies that the optical depth is inversely proportional to the photoionization rate: $\tau \propto \Gamma^{-1}$. The addition of flux from the foreground QSO decreases the optical depth by a factor $(1 + \omega)$, where ω is the ratio of the ionization rate from the foreground QSO, Γ_f , to the diffuse background ionization rate, Γ_{bkg} . Here, we give the equations to calculate Γ_f , and in the following subsection we describe the background ionization rate that we employ.

We assume for now that the luminosity, $L_f(\nu)$, of the foreground QSO is constant and isotropic. The flux along the line of sight to the background QSO is then $\mathbf{f}_f(\nu, z) = L_f(\nu)/[4\pi R_f^2(z)]$, where ν is the rest-frame frequency, and $R_f(z)$ is the proper distance between the foreground QSO and the point where the flux is measured given by:

$$R_f = \sqrt{R_\perp^2 + R_\parallel^2}, \quad (2)$$

where R_\perp is the impact parameter from Table 1, and

$$R_\parallel \equiv \frac{c}{H(z_f)} \frac{z - z_f}{1 + z_f} \equiv \frac{\Delta \mathbf{v}}{H(z_f)}. \quad (3)$$

Because R_f is small, we have neglected the redshift correction to the flux $\mathbf{f}_f(\nu, z)$. The luminosity of the foreground QSO is $L_f(\nu) = 4\pi d_L^2(z_f) \mathbf{f}_f(\nu_0, 0)$, where $d_L(z_f)$ is the luminosity distance, and $\mathbf{f}_f(\nu_0, 0)$ is the observed flux at $\nu_0 = \nu/(1 + z_f)$. We extrapolate our continuum fit to obtain the observed flux at the rest-frame Lyman limit, $\nu_H = 13.6\text{eV}$. This value can be found in Table 3, along with the Lyman limit luminosity, for each foreground QSO. In addition, the Lyman limit flux at closest separation, $\mathbf{f}_f(\nu_H, z_f)$, is written in Table 1. The ionizing flux beyond the Lyman limit

Pair	Foreground Spectrum	i^*	$\mathbf{f}_f(1460, 0)$	a_λ	$\mathbf{f}_f(\nu_H, 0)$	$L_f(\nu_H)$	$\omega(z_f)$
1	spSpec-51900-0278-203	19.28	2.75	1.67 ± 0.07	4.23	5.41	93.7
2	spSpec-51666-0300-461	19.34	3.42	1.36 ± 0.05	3.84	4.14	12.6
3	spSpec-51821-0384-338	18.46	13.0	1.87 ± 0.01	9.18	4.56	13.3

Table 3. *Column 2:* foreground QSO name. *Column 3:* i^* magnitude. *Column 4:* flux at rest-frame 1460 Å in $10^{-17}\text{erg/s/cm}^2/\text{Å}$ for our continuum fit (errors $\leq 2\%$). *Column 5:* spectral slope (with error). *Column 6:* flux at rest-frame Lyman limit in $10^{-28}\text{erg/s/cm}^2/\text{Hz}$, using our continuum fit. *Column 7:* luminosity at the Lyman limit in $10^{30}h^{-2}\text{erg s}^{-1}\text{Hz}^{-1}$. *Column 8:* ratio of photoionization rates, $\omega = \Gamma_f/\Gamma_{bkg}$, at the redshift of the foreground QSO.

is related to the photoionization rate by: $\Gamma_f(z) = \int_{\nu_H}^{\infty} \mathbf{f}_f(\nu, z) \sigma_H(\nu)/(h_p \nu) d\nu$, where $\sigma_H(\nu)$ is the hydrogen photoionization cross section and h_p is the Planck’s constant. Assuming that the QSO spectrum shortward of the Lyman limit can be characterized by a single power-law, $L_f(\nu) \propto \nu^{-1.57}$ (Telfer et al. 2001, for their radio-quiet sub-sample), then

$$\Gamma_f(z) = 0.21 \times 10^{-12} \text{ s}^{-1} \left(\frac{\mathbf{f}_f(\nu_H, z)}{10^{-21} \text{ ergs/s/cm}^2/\text{Hz}} \right). \quad (4)$$

The photoionization rates for each of our QSO pairs are plotted in Figure 2, as a function of the velocity separation between z_f and z . Also plotted are the ratios, $\omega \equiv \Gamma_f/\Gamma_{bkg}$, assuming the background rate in §3. The maximum ω values, at the redshift of the foreground QSO, for each pair can be found in Table 3. The largest proximity effect is expected in pair 1 where, because of the small angular separation, the high luminosity of the foreground QSO, and the relatively low background intensity, ω is expected to be as large as ~ 90 and to be substantially above one up to redshift separations of a few thousand km/s.

3. Simulation

This section describes the simulations that we use to evaluate the probability of observing a certain value of the transmitted flux, for an assumed photoionization rate enhanced by a foreground QSO calculated as described in the previous section.

We use an HPM simulation with 512^3 cells and a comoving box length of $40h^{-1}\text{Mpc}$ (for a description of HPM simulations see Gnedin & Hui 1998). From the resulting gas density, ρ_{gas} , the optical depth is calculated assuming photoionization equilibrium and using the temperature-density relation $T = 1.1 \times 10^4 (\rho_{gas}/\bar{\rho}_{gas})^{0.3} \text{ K}$. For the average gas density, $\bar{\rho}_{gas}$, we assume $\Omega_b h^2 = 0.02$ (O’Meara et al. 2001). The one free parameter is $\Gamma_{bkg}(z)$, which we set so that the average transmitted flux, \bar{F} , is in agreement with the results from Bernardi et al. in equation (1). Our effective background rate is plotted in Figure 3.

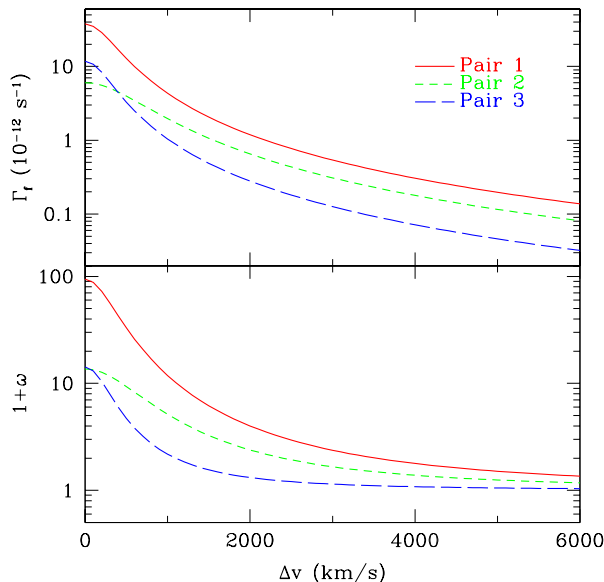


Fig. 2.— *Top*: Photoionization rate from the foreground QSOs in our sample versus velocity separation, $\Delta v \equiv c(z - z_f)/(1 + z_f)$ (the curves are essentially symmetric about $\Delta v = 0$). *Bottom*: Ratio of photoionization rate contributed by the foreground QSO to that of the background QSO, $\omega = \Gamma_f(z)/\Gamma_{bkg}$.

The density distribution in the simulation is generated from a flat CDM model with $\Omega_m = 0.4$, $h = 0.65$, $\sigma_8 = 0.83$ (consistent with cluster abundances), and primordial spectral index $n_s = 0.85$. In comparison to the power spectrum determination from the Ly α forest in Croft et al. (2002), who found an amplitude of $\Delta^2(k_p) = 0.74^{+0.20}_{-0.16}$ at $z = 2.72$ for $k_p = 0.03(\text{km s}^{-1})^{-1}$, our power spectrum has $\Delta^2(k_p) = 0.62$ [where $\Delta^2(k) = k^3 P(k)/(2\pi^2)$, and $P(k)$ is the power spectrum]. Thus, our power spectrum amplitude is on the low side of present estimates (note that Seljak, McDonald, & Makarov 2003 find that the power spectrum amplitude may be higher than found by Croft et al.). A lower amplitude of the power spectrum implies that there is more gas left in voids, hence providing more absorption over most regions in the Ly α spectrum. This means that to obtain the same mean transmitted flux, we require a *higher* value of the background photoionization rate, Γ_{bkg} . Moreover, the gas temperature we assume is on the low side of the observational determinations (Theuns et al. 2002 and references therein), and a lower temperature also leads to a higher photoionization rate because of the increased recombination coefficient. Hence our value of Γ_{bkg} is actually an upper limit inferred from the mean transmitted flux, giving a lower limit for $\omega = \Gamma_f/\Gamma_{bkg}$, and therefore making our predicted proximity effect conservatively low.

We also show in Figure 3 the measurement of Γ_{bkg} by Scott et al. (2000) from the line-of-sight proximity effect. This value is higher than our estimate by a factor of at least ~ 2 at high redshift. However, as mentioned in the introduction there are several possible systematic errors in this measurement, in particular the effect of the gas overdensity near the QSOs; see §5 below.

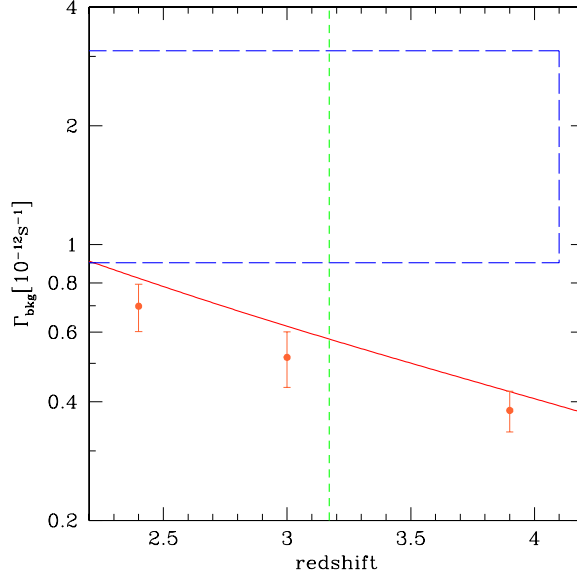


Fig. 3.— The solid line is our adopted background ionization rate. Note that in generating this background we have extrapolated the Bernardi et al. (2003) fit to τ_{eff} slightly beyond the data limits ($z = 2.6 - 4.0$). The vertical line at $z = 3.17$ shows the redshift of the simulation output we analyze. The dashed box shows the limits from Scott et al. (2000) using the line-of-sight proximity effect. The data points are from McDonald & Miralda-Escudé (2001, 2003); their lower rate compared to the one adopted here is due to their higher temperature and power spectrum amplitude, as discussed in the text.

3.1. Resolution, Pixel Size, and Noise

Once we have chosen the background, we can generate simulated spectra with and without the effect of the foreground QSO. But before comparing these to the Sloan spectra, we have to match the resolution, pixel size, and signal-to-noise of the data.

We first smooth each line of sight in the simulation separately with the average resolution quoted in Schneider et al. (2002): $\lambda/\Delta\lambda = 1950$. We then adjust the pixel size in the simulation to match the pixel size of the Sloan spectra, which is $d\mathbf{v}_{spec} = c \cdot d\lambda_o/\lambda_o = 69\text{km/s}$. The pixel size of the simulation corresponds to a velocity range of $4.9\text{km/s} (1+z)^{1/2}$, so we simply average the flux over $14 (1+z)^{-1/2}$ pixels. Finally, we add noise to the simulated spectra by adding to the transmitted flux a random number selected from a Gaussian distribution centered at zero with width equal to $N(\lambda)/\mathbf{f}_b(\lambda)$, where $N(\lambda)$ is the noise supplied for each Sloan spectrum, and $\mathbf{f}_b(\lambda)$ is our continuum fit.

4. Results

Once we have smoothed, rebinned, and added noise to our simulated spectra, we are ready to compare them to the real spectra. We make this comparison with two sets of simulated spectra: one with the background ionization rate only (“Quasar Off”), and the other with the additional ionization rate due to the foreground QSO (“Quasar On”). To test the presence of the transverse proximity effect, we plot in Figures 4, 5, and 6, for each one of our three QSO pairs, the fraction $P_{<}$ of simulated spectra in which the transmitted flux is below the measured value in the observed spectrum. If the modeling is correct, then half of the simulated spectra should have a transmitted flux below the measured one. In these plots, we have averaged the observed spectra over 5 pixels, corresponding to $\Delta v = 345 \text{ km/s}$. At this velocity separation, the $\text{Ly}\alpha$ forest correlation function is small and so the transmitted flux values in adjacent pixels are close to independent.

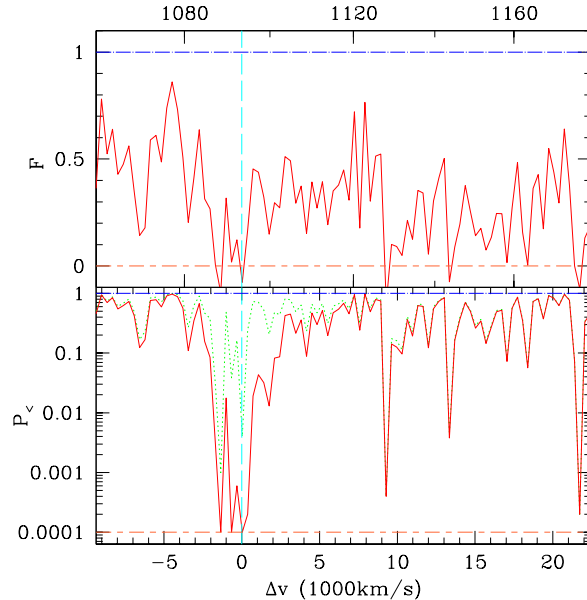


Fig. 4.— *Top*: Observed transmitted flux in the background QSO of pair 1, versus velocity separation from the foreground QSO, after rebinning the spectrum in Figure 1 over 5 pixels. *Bottom*: Fraction of 5000 simulated spectra with transmitted flux below the measured value. The dotted line assumes a uniform ionization rate, and the solid line includes the ionizing flux from the foreground QSO. If *none* of our 5000 simulated spectra have transmitted flux below the observed one, we plot the corresponding point along the dashed line at 10^{-4} .

Far from the redshift of the foreground QSOs, the probabilities $P_{<}$ are in fact not far from uniformly distributed. But in the vicinity of the foreground QSOs, the fraction of “Quasar On” spectra below the observed spectrum is very small for all three pairs. In other words, the evidence shows that the transverse proximity effect is absent in all three cases. There is no large reduction in absorption observed at the redshift of the foreground QSO as would be expected from the increased ionizing flux predicted in Figure 2. Indeed, there is actually strong $\text{Ly}\alpha$ absorption in the vicinity

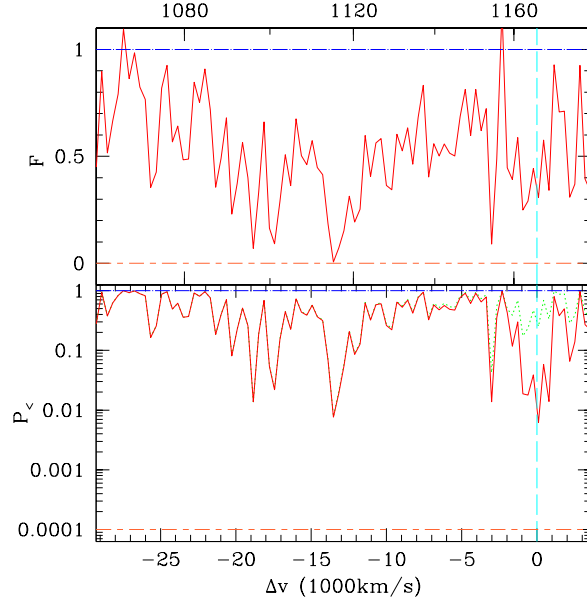


Fig. 5.— Same as Figure 4 for pair 2.

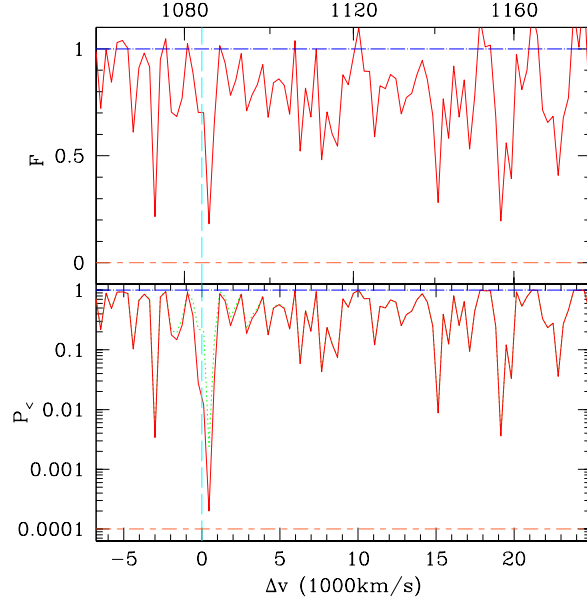


Fig. 6.— Same as Figure 4 for pair 3.

of the foreground QSO in pairs 1 and 3, and about average transmission in pair 2.

One concern is that the measured redshifts of the foreground QSOs may suffer from the same systematic uncertainties that plague the line-of-sight proximity effect. However, the SDSS redshifts do not depend on a single emission line but instead are determined by cross-correlating the continuum-subtracted spectra (see Stoughton et al. 2002) with the composite spectrum from Vanden Berk et al. (2001). For reference, the foreground QSO redshifts of pair 1, 2, 3 have, respectively,

errors of 39 km s^{-1} , 54 km s^{-1} , 136 km s^{-1} . Since these errors correspond to less than two pixels in the spectra, we will neglect them in the rest of the analysis. Even if these errors were underestimated, our visual inspection of the spectra suggests that the errors cannot be large enough to change our conclusions on the transverse proximity effect, which should be detectable over several thousands of km/s .

4.1. Discrete Absorbers

Before we proceed to discuss the possible explanations for the absence of the proximity effect, we must address a caveat with our estimate of the probability, $P_{<}$, that the transmitted flux is below the observed value, based on simulations of the $\text{Ly}\alpha$ forest spectra. In the presence of the additional ionizing flux from the foreground QSO, any optically thick absorption line will require an absorber with a high enough column density such that, even after dividing it by the factor $1 + \omega$ (in Fig. 2), the absorber still produces the low observed transmission. For example, to get the saturated absorption we see in Figure 4 for pair 1, where we have averaged over 5 pixels, would require a column density of $\sim 10^{15} \text{ cm}^{-2}$ (assuming a minimum $\text{Ly}\alpha$ optical depth of 3 over the velocity width: $\Delta v = 345 \text{ km s}^{-1}$). But if the ionizing flux has been increased by a factor $1 + \omega$ due to the proximity of a QSO, the absorber must have had a minimum column density $10^{15}(1 + \omega) \text{ cm}^{-2}$ before the QSO turned on.

However, we know that the abundance of absorbers with this high column density is underestimated by a factor of 3 to 10 in simulations similar to the one used here, because of the limited spatial and mass resolution (Miralda-Escudé et al. 1996; see also Gardner et al. 1997, 2001 for a detailed study of Lyman limit systems in simulations of different models and the effect of resolution). The probability of finding strong absorption in the simulations may therefore be too low, particularly when the flux of the foreground QSO is taken into account. Nevertheless, the probability $P_{<}$ in the pixels near the foreground QSO redshift is sufficiently small, especially in pair 1, that correcting for this would not change the high improbability that a sufficiently strong absorber just happens to be in the vicinity of the foreground QSO.

Furthermore, the high column density absorber required to produce the $\text{Ly}\alpha$ absorption at the redshift of the foreground QSO in the case of pair 1 would also need to have an unusually high velocity dispersion. In Figure 7, $P_{<}$ is replotted for the three pairs with the original pixel size (i.e., without averaging over 5 pixels). For pair 1, the low probability of the observed $\text{Ly}\alpha$ flux after the QSO ionization is taken into account (solid line) is spread over a wide velocity range of $\sim 2000 \text{ km s}^{-1}$. This very large velocity spread is rare among high column density systems (Prochaska & Wolfe 1997), and when very high velocity dispersions occur (e.g., Bahcall et al. 1996), the hydrogen column density tends to be concentrated on narrow subcomponents. Figure 8 shows the detailed SDSS spectrum of the $\text{Ly}\alpha$, $\text{Ly}\beta$, and Lyman limit absorption spectrum in pair 1, at the redshift of the foreground QSO. We see that despite the broad $\text{Ly}\alpha$ absorption line, there is no discernible Lyman limit absorption, and $\text{Ly}\beta$ absorption only shows two narrow

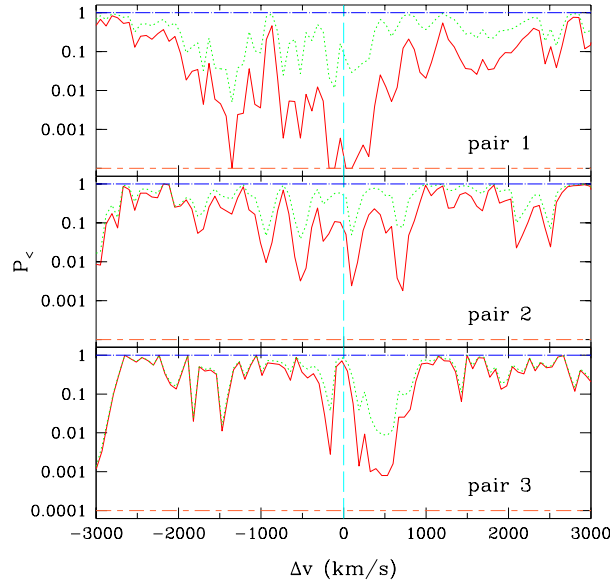


Fig. 7.— Same as bottom panels in Figures 4, 5, 6, but for single pixels in the SDSS spectra. *Solid lines*: “Quasar On” simulations. *Dotted lines*: “Quasar Off”.

subcomponents. This shows that the absorption does not arise from a few highly dense clumps in a Lyman limit system, but from gas that is well spread over the 2000 km s^{-1} velocity range. In fact, to have saturated $\text{Ly}\alpha$ absorption over this velocity range requires a minimum column density of $\sim 10^{16} \text{ cm}^{-2}$, but the total column density cannot be larger than $\sim 10^{17} \text{ cm}^{-2}$ due to the absence of Lyman limit absorption. This suggests that the absorption system is due to gas distributed over a region comparable in size to the impact parameter to the QSO. Such a large region should have been well resolved in our simulations.

For pairs 2 and 3, the absorption is less strong and the factor $1 + \omega$ is smaller, so the possibility of a coincident Lyman limit system is not as unlikely as in pair 1. We have also searched for Lyman limit absorption in pair 2, and there is none, so the strong $\text{Ly}\alpha$ absorption lines in pair 2 near the foreground QSO must have a total column density below $\sim 10^{17} \text{ cm}^{-2}$ (for pair 3, the low redshift of the foreground QSO puts the Lyman limit outside the SDSS spectrum wavelength range).

The fact that the transverse proximity effect is absent in all three of our pairs essentially rules out that the absorption is caused by random Lyman limit systems unrelated to the foreground QSOs, even if the probabilities $P_{<}$ obtained from our simulations were too low by a factor up to 10 and if we ignore the additional difficulty of the high velocity dispersion required. The evidence shows that either the gas density is greatly enhanced out to distances of ~ 1 proper Mpc from QSOs, or the QSO ionizing flux is suppressed because of variability and/or anisotropy of the emission.

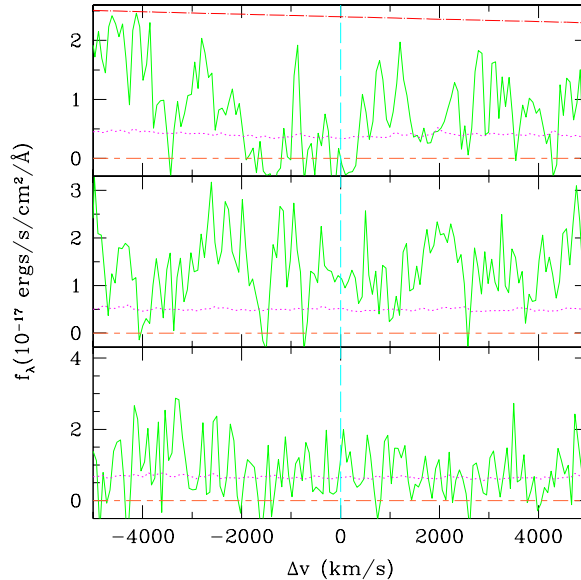


Fig. 8.— Spectrum of the background QSO in pair 1 (solid lines) centered at the redshift of the foreground QSO (vertical dashed lines) of Ly α (top panel), Ly β (middle panel), and Lyman limit (bottom panel). The dotted lines are the noise, and the dot-dashed line is the continuum fit. Note the absence of Lyman limit absorption or strong Ly β absorption near the foreground QSO redshift.

5. Clustering

We have assumed as a starting point that the average gas density in the vicinity of the foreground QSO is not different from the overall average density. There is, however, reason to believe that there is a density enhancement around both radio-loud and radio-quiet QSOs from the galaxy-QSO clustering that is observed (see Ellingson, Green & Yee 1991; Hutchings et al. 1995; McLure & Dunlop 2001; Wold et al. 2001; Finn et al. 2001) and has been modeled (Kauffman & Haehnelt 2002). This density enhancement would result in excess absorption, diminishing the signature of the proximity effect due to the ionizing radiation, which would lead to an *over-estimate* of the background ionization rate (see Fig. 3). Pascarelle et al. (2001) attempted to use the observed QSO-galaxy correlation to correct the ionizing background intensity inferred from the proximity effect, but their conclusions depend on their assumption that all Ly α lines originate in fixed gaseous halos around galaxies, and they neglected peculiar velocity effects.

A gas density enhancement would also be expected around Lyman-Break Galaxies (LBGs). Adelberger et al. (2003) found that the mean transmitted flux decreases near an LBG, dropping from a mean value of 0.67 at large distances to ~ 0.55 at $0.5h^{-1}$ proper Mpc, at $z = 3$.² Using

²Adelberger et al. also find high transmitted flux within $0.125h^{-1}$ Mpc (proper) from LBGs, which they attribute to galactic wind effects, but this distance is much smaller than those probed by our QSO pairs.

our simulations, we find that this decrease in mean transmitted flux corresponds to an increase in the optical depth by a factor of ~ 2 . The optical depth in pair 1 is expected to decrease from the enhanced photoionization rate by a factor of $(1 + \omega)^{-1} \sim 1/90$ at this separation, so if the gas density enhancement around LBGs and luminous QSOs were the same, it could not explain the lack of a proximity effect in our data. Nevertheless, QSOs may generally inhabit more massive halos than do LBGs, placing them in dense environments of a larger scale.

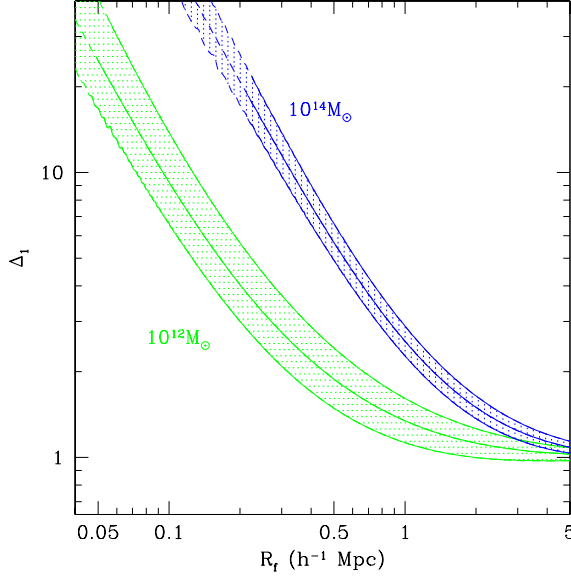


Fig. 9.— The non-linear overdensity Δ_1 at a proper radius R_f around collapsed structures of mass $10^{12} M_\odot$ and $10^{14} M_\odot$ at $z = 4$. The shaded regions bracket the one sigma deviation in initial overdensity. The solid lines turn to dashed lines when the radius has passed below the virial radius, where we imagine the overdensity will diverge from the spherical collapse model.

Without an appropriate empirical estimate of the gas clustering around QSOs, we will attempt to model it analytically, following the calculations in Loeb & Eisenstein (1995). As outlined in the Appendix, we calculate (by assuming Gaussian fluctuations and the spherical collapse model) the non-linear matter overdensity Δ_1 at proper radius R_f corresponding to the average density perturbation around a halo (see Fig. 9), and we assume that the gas traces the matter, i.e., $\Delta_1 = \rho_{gas}/\bar{\rho}_{gas}$. This gas overdensity will affect the neutral hydrogen density through the relation: $\rho_{HI} \propto \rho_{gas}^2 \alpha(T)$, where $\alpha(T) \propto T^{-0.7}$ is the recombination coefficient. For $T \propto \rho_{gas}^{0.3}$, this implies $\rho_{HI} \propto \rho_{gas}^{1.79}$, and including also the effects of peculiar velocities, the optical depth will increase by:

$$1 + \omega_{cl} = \Delta_1^{1.79} \left| \left(1 + \frac{d\mathbf{v}_{pec}}{H d\ell} \right)^{-1} \right|, \quad (5)$$

where $d\ell$ is the space line element. Note that caustics on ω_{cl} appear when $d\mathbf{v}_{pec}/d\ell = -H$, and inside the caustics we need to add the contribution to $1 + \omega_{cl}$ from multiple points in space to the

same observed wavelength. The peculiar velocities shift the wavelength at which we observe the absorption, thereby changing equation (3) to

$$R_{\parallel} = \frac{\Delta v - v_{pec}}{H(z_f)} . \quad (6)$$

Because v_{pec} has the opposite sign of R_{\parallel} (see Appendix), absorption observed at a redshift separation Δv will be located at a distance $R_f = (R_{\perp}^2 + R_{\parallel}^2)^{1/2}$, which is in general farther than in the absence of peculiar velocities. The larger inferred distance for a given Δv implies that the expected flux from the QSO, as well as the clustering effect due to the enhanced gas density, are reduced.

We show in Figure 10 as solid lines the ratio $(1 + \omega_{cl})/(1 + \omega)$, for pair 1, where $1 + \omega$ is the factor by which the optical depth is suppressed due to the increased ionizing flux, and $1 + \omega_{cl}$ is the factor by which the optical depth is increased by the enhanced gas density, according to equation (5). The three panels assume that the QSO is in the center of a halo with mass of $(10^{14}, 10^{13}, 10^{12}) M_{\odot}$, with the mean density profile of Figure 9. The dotted line shows the same ratio when peculiar velocities are not included, and the dashed line shows $1/(1 + \omega)$, i.e., the effects of photoionization only, also with no peculiar velocities. Note that for a halo mass $10^{13} M_{\odot}$, the line of sight to the background QSO in pair 1 just grazes the turnaround radius of the halo around the foreground QSO, producing the high central caustic.

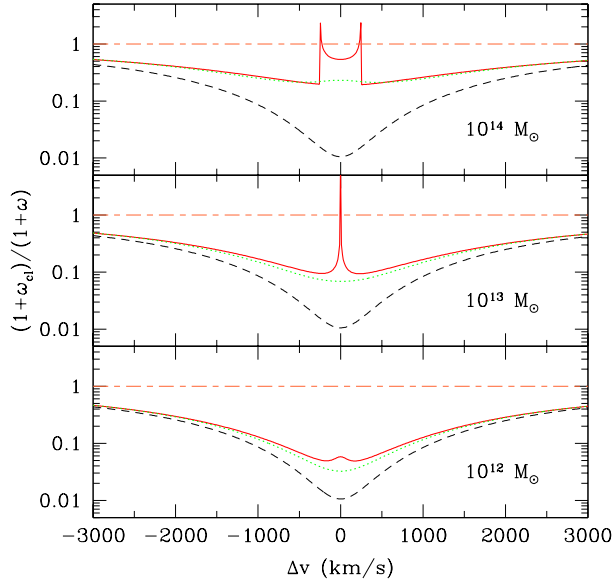


Fig. 10.— *Solid lines*: Ratio of the clustering effect (eq. 5) to the radiation effect (Fig. 2) in pair 1 for halo masses of $10^{14} M_{\odot}$ (top), $10^{13} M_{\odot}$ (middle), and $10^{12} M_{\odot}$ (bottom). *Dashed line*: Photoionization effect only, shown as $(1 + \omega)^{-1}$. *Dotted line*: Ratio without including the effect from the peculiar velocities.

We see that the effects of clustering are important and they can partly compensate for the

increased ionizing flux. However, even for a halo mass of $10^{14} M_{\odot}$, the total factor by which the optical depth is changed by the combined effects of photoionization and clustering is still substantially less than unity, except in the narrow region between the velocity caustics within $\sim 250 \text{ km s}^{-1}$ of the QSO redshift. As mentioned earlier, the peculiar velocities decrease both $1 + \omega_{cl}$ and $1 + \omega$, but their ratio is only slightly modified outside the velocity caustics.

Plausible values of the mass of the halo around the QSO can be constrained by the mass of the black hole required to power the QSO, and by comparing the abundance of halos with the abundance of QSOs. A lower limit to the black hole is obtained by assuming that the luminosity is equal to the Eddington luminosity, in which case:

$$\frac{M_{\bullet}}{M_{\odot}} \simeq 10^{-0.4M_B - 1.6} \quad (7)$$

where $\sim 10\%$ of the emission is assumed to be in the B band (see Elvis et al. 1994). For the magnitude of the foreground QSO in pair 1, $M_B = -26.9$,³ we have $M_{\bullet} \sim 10^9 M_{\odot}$. Similar mass estimates can be made for the foreground QSO in pair 2 ($M_B = -26.7$) and pair 3 ($M_B = -26.4$). If we assume the typical black hole to bulge mass ratio of 0.13% (Merritt & Ferrarese 2001) and assume the bulge to halo mass ratio is of order the baryon fraction ($\sim 10\%$), then we obtain a halo mass, M_h , of roughly $10^{13} M_{\odot}$.

The surface density of halos per unit redshift has been plotted in Figure 11 using the Press-Schechter formalism (Press & Schechter 1974). At the redshift of pair 1 ($z = 4$), there are (1000, 10, 0.001) halos per deg^2 with (10^{12} , 10^{13} , 10^{14}) M_{\odot} , respectively. We can compare this to the 0.2 QSOs per deg^2 in the Early Data Release at the same redshift.⁴ This means that it is highly unlikely that the foreground QSO in pair 1 may reside in a $10^{14} M_{\odot}$ halo. However, the overdensity around smaller mass halos is apparently not sufficient to offset the purported flux from the foreground QSO. As shown in Figure 10, the effect of clustering is too small to eliminate the effect of the extra radiation in pair 1 except for the region between the caustics, with a width of only $\Delta v \sim 500 \text{ km s}^{-1}$ even for the case $M_h = 10^{14} M_{\odot}$. For a $10^{13} M_{\odot}$ halo (a more likely mass given the halo abundances), the region between caustics has practically disappeared and the optical depth should still be decreased by a factor of 5 to 10 over most of the region in which excess absorption is observed ($-1500 \text{ km s}^{-1} < \Delta v < 500 \text{ km s}^{-1}$ in Fig. 7).

For the other two pairs, we have plotted the clustering/radiation ratio in Figure 12, assuming a $10^{13} M_{\odot}$ halo. In the case of pair 2, the clustering again appears to be insufficient for offsetting the ionizing flux from the foreground QSO. As for pair 3, it is possible that the reduced absorption that we expected from the transverse proximity effect has been mitigated by the enhanced density

³We derive the absolute B magnitude from the given i^* magnitude, assuming $L_{\nu} \propto \nu^{-0.44}$ from the composite spectrum in Vanden Berk et al. (2001).

⁴There are 482 QSOs with $z > 2.2$ and 91 with $3.5 > z > 4.5$ over a field of 494 deg^2 .

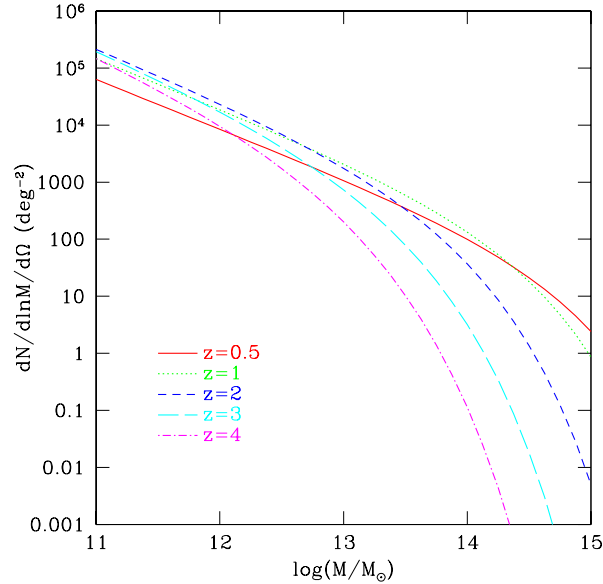


Fig. 11.— The surface density per deg^2 of halos of a given mass per unit redshift from the Press-Schechter formalism. Note that the cosmology assumed is the same as in the simulation: $(\Omega_m, \Omega_\Lambda, h, \sigma_8, n_s) = (0.4, 0.6, 0.65, 0.83, 0.85)$.

around the foreground QSO. However, it might remain difficult to explain the wide absorption feature seen in Figure 7 at $\sim 500 \text{ km s}^{-1}$ if indeed the expected excess radiation is impinging on that region of the IGM. In any case, clustering by itself appears to be unable to account for the lack of a transverse proximity effect in all three pairs. The alternatives, which we address in the next sections, are QSO variability and anisotropy.

6. QSO anisotropy

A different possibility to explain the lack of a transverse proximity effect is that the emission from QSOs is highly anisotropic. In any flux limited survey, the observed QSOs would be preferentially observed along directions in which they appear particularly bright, and their flux seen along other directions could be much lower.

The angle, ϕ , that a given redshift separation corresponds to is plotted in the top two panels of Figure 13. In the case of pair 1, the QSO flux would have to be obscured from roughly $\phi \simeq 10^\circ$ to $\phi \simeq 150^\circ$ to explain the low probability region between $\Delta v = -1500 \text{ km s}^{-1}$ and $\Delta v = 500 \text{ km s}^{-1}$. If we assume that this obscuration is symmetric around an axis, then the half-opening angle would only be $\sim 20^\circ$. As shown in Figure 13, peculiar velocities would have a only a small effect on this angle. For pairs 2 and 3, a wider half-opening angle ($\sim 40^\circ - 50^\circ$) is allowed because of the larger impact parameter and the lower velocity range in the spectrum in which the probability $P_<$ is very low.

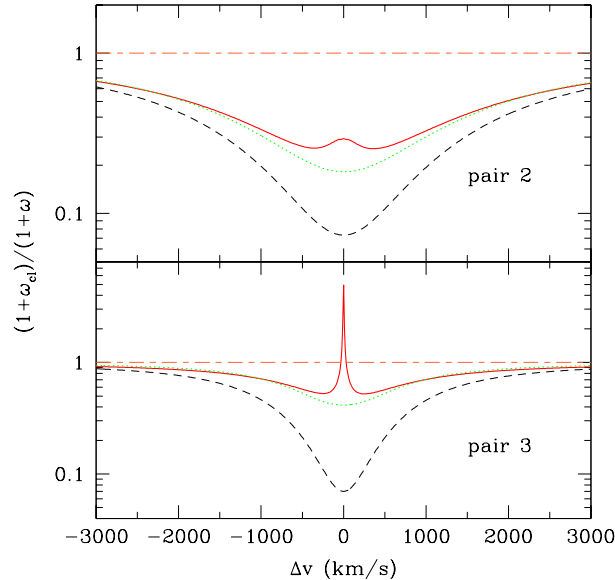


Fig. 12.— Ratio of the clustering effect to the radiation effect as in Figure 10, but here for pair 2 (*top*) and pair 3 (*bottom*), assuming for both a halo of $10^{13} M_{\odot}$.

A beam radius as small as 20° for the QSO radiation seems implausible. In unified models of AGN, the continuum ionizing radiation is supposed to come from the accretion disk, which may be absorbed by an obscuring torus near the equator, but typical half-opening angles are $\sim 30^{\circ} - 45^{\circ}$ (Antonucci 1993; Schmitt et al. 2001), and they are thought to increase with luminosity (Rudge & Raine 2000). A separate possibility is that the QSO has not ionized the gas in its host halo, and that the ionizing radiation is able to escape only along a narrow tunnel among clouds. However, the fact that most QSOs of luminosity similar to the foreground one in pair 1 do not exhibit intrinsic Lyman limit absorption in their spectrum implies that this explanation could not account for a narrow beam of emission in most QSOs.

To summarize, beaming of the ionizing radiation might be one of the reasons for the absence of the transverse proximity effect in our three pairs, but if this absence is generally confirmed on a larger sample of pairs, then beaming alone cannot be the sole explanation.

7. QSO variability

The final effect we consider is the possibility that the QSO flux is variable. There is a time delay between the emission of the QSO flux that we observe at present and the emission of the QSO flux that illuminated the hydrogen in the spectrum of the background QSO, given by $\Delta t \simeq \frac{1}{c}(R_f + R_{\parallel})$, where R_f and R_{\parallel} are defined in equations (2) and (3). The time-delay is plotted in the bottom two panels of Figure 13 for all three pairs. The dotted curve shows the effect of including peculiar velocities when the foreground QSO in pair 1 is in a halo of mass $10^{13} M_{\odot}$.

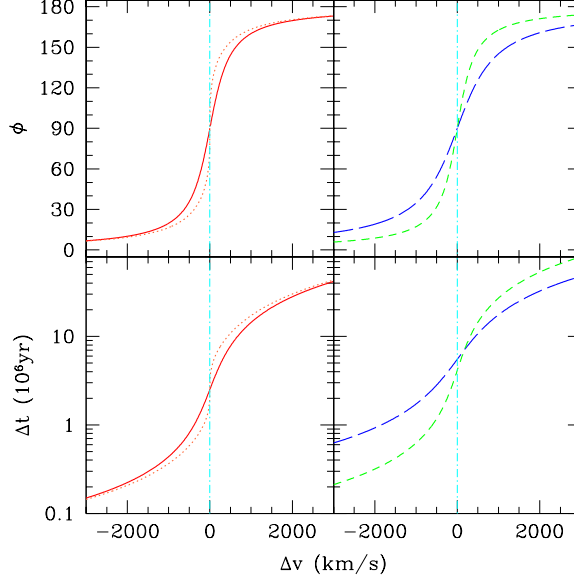


Fig. 13.— *Top left*— The angle, ϕ , between the line of sight to the foreground QSO and the line connecting the QSO to the point at Δv in pair 1. The *solid* line assumes no clustering, whereas the *dotted* line assumes the foreground QSO is in a halo of $10^{13} M_{\odot}$. We plot both cases to show the effect of the induced peculiar velocities. *Top right* — The angle, ϕ , for pair 2 (*long dash*) and pair 3 (*short dash*) without clustering. *Bottom left and right*— The delay between the time when the QSO emits the light we see and the time when the QSO emits the light impinging on the point at Δv . The lines are the same as above.

We again focus on the region $-1500 \text{ km s}^{-1} < \Delta v < 500 \text{ km s}^{-1}$ in pair 1 where the probability $P_{<}$ is lowest. If the lack of a proximity effect were due to the time-delay only, we find by comparing Figures 2 and 13 that the QSO luminosity would need to have been ~ 10 times lower than now at a time 3×10^5 years ago, and 50 to 100 times lower than now over the period from 10^6 to 10^7 years ago. In the case of pairs 2 and 3, the QSOs would have to be shining an order of magnitude less bright from $\sim 2 \times 10^6$ to 10^7 years ago. These required variations in the luminosities would be smaller if significant clustering existed around the QSO (Figs. 10 and 12).

There are other measurements related to the proximity effect that are sensitive to the time interval over which QSOs maintain their luminosity. The existence of the line-of-sight proximity effect requires that the QSOs shine continuously for a photoionization timescale, which is $\sim 3 \times 10^4$ years for the measured ionizing background intensity (see the introduction). The case of Q0302-003, and its Ly α void associated with another nearby QSO, analyzed by Dobrzycki & Bechtold (1991), requires a lifetime longer than 10^7 years if the void is really caused by the QSO. The same QSO, Q0302-003, was observed in the He II Ly α spectrum by Jakobsen et al. (2003), who found a gap in the absorption associated with another QSO near the line of sight. The required QSO lifetime is also 10^7 years if the QSO is responsible for the gap. The large H II region around a $z=6.28$ QSO also requires a lifetime longer than 10^7 years if it was entirely ionized by the QSO (Pentericci et

al. 2002; Haiman & Cen 2002).

We point out here another argument that shows that many luminous QSOs must sustain their luminosities for periods of at least 10^7 years. Of the four QSOs on which the He II Ly α intergalactic absorption has been observed, two show a strong line of sight proximity effect: Q0302-003, and PKS1935 (Anderson et al. 1999, Heap et al. 2000). The observed flux of these QSOs of $\sim 2 \times 10^{-16} \text{ erg cm}^{-2} \text{ s}^{-1} \text{ \AA}^{-1}$ implies a photon luminosity of $\sim 10^{56} \text{ s}^{-1}$ in photons that can ionize He II (i.e., with energy greater than 54 eV). The size of the proximity effect in the spectra of these two QSOs is $\Delta z \simeq 0.08$, or a proper distance of 20 Mpc. With this luminosity and at this distance, the photoionization rate on He II ions that is obtained is $\sim 10^{-7} \text{ yr}^{-1}$. If the QSO had been shining for a time less than 10^7 years, it could not have ionized the region in which the proximity effect is observed to the level implied by its luminosity (see Anderson et al. 1999). We note that this argument does not require the assumption that the QSO *ionized* the entire He III region, but only that the QSO has maintained its ionization over the last photoionization timescale.

It is worth mentioning here that one must distinguish between the total length of time during which a black hole is producing a certain luminosity as it accretes, and the continuous time interval over which a QSO maintains its luminosity. QSOs might have repeated episodes of high luminosity, each one relatively short and separated by intervals of lower luminosity, which could add up to a longer total time of emission. Several papers (Fabian & Iwasawa 1999; Barger et al. 2001; Yu & Tremaine 2002; Haehnelt 2003) have shown that the total mass density of nuclear black holes in the universe is comparable to the mass density inferred from the radiation background from QSOs (Soltan 1982), for an assumed radiative efficiency of the accreted matter: $\epsilon \sim 10\%$. This also implies that, if QSOs generally emit near the Eddington luminosity, L_{Edd} , then their total time of emission is $L_{Edd}/(M_{\bullet} c^2 \epsilon) \simeq 4 \times 10^7$ years. Measurements based on the amplitude of QSO clustering and the assumption that QSOs are located in massive halos (Martini & Weinberg 2001; Martini 2003) also measure this total time of emission.

In conclusion, we have found that although the time-delay effect can explain the absence of the proximity effect, it requires the foreground QSO in pair 1 to be younger than 10^6 years, and the lifetime should be $< 2 \times 10^6$ years for pairs 2 and 3 (owing to their larger impact parameters). At the same time, there is evidence that other QSOs have sustained their luminosities for much longer times. Therefore, time-delays can only eliminate the transverse proximity effect in some QSOs if there is a wide range of variation in the time intervals over which QSOs remain at a high luminosity.

8. Conclusion

We have found three sets of SDSS QSO pairs in which we expected to see evidence for the transverse proximity effect. The fact that we do not implies that either the gas density along the line of sight is much higher than average, or the ionizing flux expected from the observed QSO is

suppressed.

Although it is likely that the high-redshift, luminous QSOs are located near the center of the most massive halos that exist at the time when they are observed, we have found that the gas density enhancement is not sufficient to fully compensate for the increased ionizing intensity from the QSO. For reasonable halo masses that are consistent with the abundance of QSOs, the impact parameters in our QSO pairs are similar or larger than the radius around the halo where gas is just turning around, and the overdensity is not large. This suggests that there must also be a reduction of the QSO flux, either due to anisotropic emission or to a lower luminosity of the QSO in the past 3×10^5 to 10^7 years. Each one of these two explanations also has problems to account for the absence of a transverse proximity effect in three pairs by itself: anisotropy requires a very small opening angle, and variability implies a large reduction of the luminosity over a timescale over which other QSOs are known to have remained highly luminous (Jakobsen et al. 2003). The combination of the three effects (high gas density around the QSOs, anisotropy and variability) can probably more easily account for the observed Ly α excess absorption near the foreground QSOs, rather than the excess transmission that was expected.

Previous studies have also generally found no evidence for the transverse proximity effect. Crotts & Fang (1998) found, just as we do, excess Ly α absorption compared to the mean transmitted flux in the region of the proximity effect. Møller & Kjærgaard (1992) concluded from an analysis of one pair and the triplet of QSOs from Crotts (1989) that the transverse flux from local QSOs had to be reduced by a factor of at least 0.22 for an assumed background photoionization rate $\Gamma_{bkg} \simeq 3 \times 10^{-12} \text{ s}^{-1}$. For our lower assumed values of Γ_{bkg} (Fig. 3), this corresponds to a reduction factor ~ 0.05 . Fernández-Soto et al. (1995) detected in 3 pairs a weak transverse proximity effect that was consistent with a high value of the background ionization rate, $\Gamma_{bkg} \simeq 10^{-11} \text{ s}^{-1}$. Assuming this rate is an order of magnitude too large, we can interpret the small observed effect as due to a reduction in the transverse flux by a factor of 0.1. To express our results in terms of a reduction factor, we can assume that the probability $P_{<}$ for all points in Figure 7 should, minimally, be greater than 0.001. To obtain this, we find the transverse flux in pair 1 must be less than 0.07 times the expected isotropic value. The fact that many of the closest pairs in the literature exhibit at least a 10% reduction in the transverse flux considerably strengthens our conclusion.

Future progress in understanding the proximity effect should come from a reanalysis of the line-of-sight proximity effect in a large sample of QSOs. An enhanced gas density near QSOs should equally impact the proximity effect on the line of sight, and although its strength is complicated by the effect of peculiar velocities this can be modeled in simulations. The environment of QSOs can be probed not only from the average proximity effect, but also from its scatter. It is well known that the value of the ionizing background intensity inferred from the proximity effect varies widely from one QSO to another, implying that a large sample must be used; however, this scatter is probably not explained by the Ly α absorption variance in random regions of the intergalactic medium, and the effect of the QSO environment is likely to be important.

A thorough investigation of the line-of-sight proximity effect should help in disentangling the effects of gas density and the reduction of the QSO flux in the transverse proximity effect. The effects of anisotropy and variability can hopefully also be separated, once a large number of pairs over a range of angular separations are available. The flux reduction due to anisotropy should depend only on the angle ϕ (see §6) and not the distance to the QSO, and should be symmetric when changing ϕ to $\pi - \phi$ (except if the two QSO “beams” are often of different luminosity), whereas the mean reduction due to variability should be a monotonically increasing function of time delay. There is a promising potential in the transverse proximity effect for learning on the environment, anisotropy, and variability of QSOs.

Acknowledgements. We thank Gordon Richards for supplying us with the list of high redshift SDSS QSOs. We also thank James Bullock, Juna Kollmeier, Smita Mathur, Pat Osmer, Rick Pogge, Terry Walker, David Weinberg, and Andrew Zentner for helpful discussions. We acknowledge support from U.S. DOE Contract No.DE-FG02-91ER40690 for MS, and from NSF grant NSF-0098515 for JM. The numerical simulations used in this paper were performed at NCSA.

REFERENCES

- Adelberger, K. L., Steidel, C. C., Shapley, A. E., & Pettini, M. 2003, *ApJ*, 584, 45
- Anderson, S. F., Hogan, C. J., Williams, B. F., & Carswell, R. F. 1999, *AJ*, 117, 56
- Antonucci, R. 1993, *ARA&A*, 31, 473
- Bahcall, J. N. et al. 1996, *ApJ*, 457, 19
- Bajtlik, S., Duncan, R., & Ostriker, J. P. 1988, *ApJ*, 327, 570
- Barger, A. J., Cowie, L. L., Bautz, M. W., Brandt, W. N., Garmire, G. P., Hornschemeier, A. E., Ivison, R. J., & Owen, F. N. 2001, *AJ*, 122, 2177
- Bernardi, M. et al. 2003, *AJ*, 125, 32
- Carswell, R. F., Whelan, J. A. J., Smmith, M. G., Boksenberg, A., & Tytler, D. 1982, *MNRAS*, 198, 91
- Croft, R. A. C., Weinberg, D. H., Bolte, M., Burles, S., Hernquist, L., Katz, N., Kirkman, D., & Tytler, D. 2002, *ApJ*, 581, 20
- Crotts, A. P. S. 1989, *ApJ*, 336, 550
- Crotts, A. P. S., & Fang, Y. 1998, *ApJ*, 502, 16
- Dobrzycki, A. & Bechtold, J. 1991, *ApJ*, 377, L69
- Ellingson, E., Green, R. F., & Yee, H. K. C. 1991, *ApJ*, 378, 476

- Elvis, M. et al. 1994, *ApJS*, 95, 1
- Fabian, A. C., & Iwasawa, K. 1999, *MNRAS*, 303, L34
- Fernández-Soto, A., Barcons, X., Carballo, R., & Webb, J. K. 1995, *MNRAS*, 277, 235
- Finn, R. A., Impey, C. D., & Hooper, E. J. 2001, *ApJ*, 557, 578
- Gardner, J. P., Katz, N., Hernquist, L., & Weinberg, D. H. 1997, *ApJ*, 484, 31
- Gardner, J. P., Katz, N., Hernquist, L., & Weinberg, D. H. 2001, *ApJ*, 559, 131
- Gnedin, N. Y. & Hui, L. 1998, *MNRAS*, 296, 44
- Haehnelt, M. G. 2003, *ArXiv Astrophysics e-prints*, 7378
- Haiman, Z. & Cen, R. 2002, *ApJ*, 578, 702
- Heap, S. R., Williger, G. M., Smette, A., Hubeny, I., Sahu, M. S., Jenkins, E. B., Tripp, T. M., & Winkler, J. N. 2000, *ApJ*, 534, 69
- Hutchings, J. B., Crampton, D., & Johnson, A. 1995, *AJ*, 109, 73
- Jakobsen, P., Jansen, R. A., Wagner, S., & Reimers, D. 2003, *A&A*, 397, 891
- Kauffmann, G. & Haehnelt, M. G. 2002, *MNRAS*, 332, 529
- Liske, J. & Williger, G. M. 2001, *MNRAS*, 328, 653
- Loeb, A. & Eisenstein, D. J. 1995, *ApJ*, 448, 17
- Martini, P. & Weinberg, D. H. 2001, *ApJ*, 547, 12
- Martini, P. 2003, *ArXiv Astrophysics e-prints*, 4009
- McDonald, P., Miralda-Escudé, J., Rauch, M., Sargent, W. L. W., Barlow, T. A., Cen, R., & Ostriker, J. P. 2000, *ApJ*, 543, 1
- McDonald, P. & Miralda-Escudé, J. 2001, *ApJ*, 549, L11
- McDonald, P. & Miralda-Escudé, J. 2003, submitted to *ApJ* (erratum to *ApJ*, 549, L11)
- McLure, R. J. & Dunlop, J. S. 2001, *MNRAS*, 321, 515
- Merritt, D. & Ferrarese, L. 2001, *MNRAS*, 320, L30
- Miralda-Escudé, J., Cen, R., Ostriker, J. P., & Rauch, M. 1996, *ApJ*, 471, 582
- Møller, P. & Kjærgaard, P. 1992, *A&A*, 258, 234

- Murdoch, H. S., Hunstead, R. W., Pettini, M., & Blades, J. C. 1986, *ApJ*, 309, 19
- O’Meara, J. M., Tytler, D., Kirkman, D., Suzuki, N., Prochaska, J. X., Lubin, D., & Wolfe, A. M. 2001, *ApJ*, 552, 718
- Pascarelle, S. M., Lanzetta, K. M., Chen, H., & Webb, J. K. 2001, *ApJ*, 560, 101
- Pentericci, L. et al. 2002, *AJ*, 123, 2151
- Press, W. H., Rybicki, G. B., & Schneider, D. P. 1993, *ApJ*, 414, 64
- Press, W. H. & Schechter, P. 1974, *ApJ*, 187, 425
- Prochaska, J. X., & Wolfe, A. M. 1997, *ApJ*, 487, 73
- Rauch, M. 1998, *ARA&A*, 36, 267
- Rauch, M., Miralda-Escudé, J., Sargent, W. L. W., Barlow, T. A., Weinberg, D. H., Hernquist, L., Katz, N., Cen, R., & Ostriker, J. P. 1997, *ApJ*, 489, 7
- Rudge, C. M. & Raine, D. J. 2000, *MNRAS*, 311, 621
- Schirber, M. & Bullock, J. S. 2003, *ApJ*, 584, 110
- Schmitt, H. R., Antonucci, R. R. J., Ulvestad, J. S., Kinney, A. L., Clarke, C. J., & Pringle, J. E. 2001, *ApJ*, 555, 663
- Schneider, D. P. et al. 2002, *AJ*, 123, 567
- Scott, J., Bechtold, J., Dobrzycki, A., & Kulkarni, V. P. 2000, *ApJS*, 130, 67
- Seljak, U., McDonald, P., & Makarov, A. 2003, *ArXiv Astrophysics e-prints*, 2571
- Soltan, A. 1982, *MNRAS*, 200, 115
- Stoughton, C., et al. 2002, *AJ*, 123, 485
- Tegmark, M. & Zaldarriaga, M. 2002, *Phys. Rev. D*, 66, 103508
- Telfer, R. C., Zheng, W., Kriss, G. A., & Davidsen, A. F. 2002, *ApJ*, 565, 773
- Theuns, T., Zaroubi, S., Kim, T.-S., Tzanavaris, P., & Carswell, R. F. 2002, *MNRAS*, 332, 367
- Vanden Berk, D. E. et al. 2001, *AJ*, 122, 549
- Wold, M., Lacy, M., Lilje, P. B., & Serjeant, S. 2001, *MNRAS*, 323, 231
- Yu, Q. & Tremaine, S. 2002, *MNRAS*, 335, 965

9. Appendix

To determine the overdensity as a function of radius outside a collapsed object, we assume the spherical collapse model to determine the evolution of the proper radius R of a shell containing a constant mass M , which is parameterized as:

$$R = \frac{R_{ta}}{2}(1 - \cos(\eta)), \quad t = \frac{t_{ta}}{\pi}(\eta - \sin(\eta)) \quad (8)$$

where “ ta ” stands for *turnaround*, i.e., the point of maximum expansion for a particular shell. We assume that the foreground QSO is at the center of a halo with mass M_h collapsed at the time we are viewing the QSO, at redshift z_f . In the standard top-hat spherical model, this implies that the mean linear overdensity inside the comoving radius $r_h \equiv [3M_h/(4\pi\bar{\rho}_{m,0})]^{1/3}$ (where $\bar{\rho}_{m,0}$ is the mean comoving matter density) is $\bar{\delta}_h = 1.69$ (assuming $\Omega_m = 1$, valid at high redshift). To evaluate the average overdensity around the halo, we follow the method of Loeb & Eisenstein (1995). At a comoving radius $r_1 > r_f$, the normalized average linear density fluctuation is $\nu_1 \equiv \bar{\delta}_1/\sigma_M(r_1, z_f)$, where $\sigma_M(r_1, z_f)$ is the rms fluctuation $\delta M/M$ on a sphere of radius r_1 , and $\bar{\delta}_1$ is the mean linear overdensity within radius r_1 around the halo of mass M_h . The mean and the variance of the distribution of ν_1 are $\gamma_{h1} \cdot \nu_h$ and $1 - \gamma_{h1}^2$, respectively, where $\nu_h \equiv \bar{\delta}_h/\sigma_M(r_h, z_f)$ and

$$\gamma_{h1} = \frac{1}{2\pi^2\sigma_M(r_h)\sigma_M(r_1)} \int_0^\infty k^2 dk P(k) W(k \cdot r_h) W(k \cdot r_1) . \quad (9)$$

Here, $W(x) = 3j_1(x)/x$ is the Fourier window function for a top-hat filter, and j_1 is a spherical Bessel function.⁵

We next solve for the non-linear overdensity $\Delta_1 \equiv \rho_m(R_1)/\bar{\rho}_m$, where $\rho_m(R_1)$ is the proper matter density at the radius R_1 implied by the linear overdensity $\bar{\delta}_1$, and $\bar{\rho}_m = \bar{\rho}_{m,0}(1 + z_f)^3$. The turnaround radius and turnaround time of the shell at r_f are (in a flat cosmology)

$$R_{ta,1} = R_{ta,h} \frac{r_1 \bar{\delta}_h}{r_h \bar{\delta}_1}, \quad t_{ta,1} = t_{ta,h} \left(\frac{\bar{\delta}_1}{\bar{\delta}_h} \right)^{-3/2}. \quad (10)$$

We solve for η_1 in equations (8) by equating the time variable for the shells at r_h and r_1 , and then find the radius R_1 of the shell in the non-linear evolution. Note that R_1 is the same as R_f from equation (2). The non-linear overdensity is

$$\Delta_1 = \left(\frac{r_1}{R_1} \right)^2 \frac{dr_1}{dR_1} (1 + z_f)^{-3}. \quad (11)$$

⁵Eq. 8 in Loeb & Eisenstein (1995) appears to be missing a factor of $3/(\sqrt{2}\pi)$. This assures that $\gamma_{h1} = 1$ for $r_h = r_1$.

We have plotted this overdensity in Figure 9 for two mass scales, $10^{12}M_{\odot}$ and $10^{14}M_{\odot}$, and we assume in equation (5) that the gas overdensity is equal to the matter overdensity. The velocity of the shell in the reference frame of the center of the sphere is:

$$\mathbf{v}_1 \equiv \frac{dR}{dt} = \pm H r_1 \sqrt{1 - \frac{R_1}{R_{ta,1}}} \left(\frac{r_1}{R_1} \right)^{1/2} (1 + z_f)^{-3/2} \quad (12)$$

where by definition we make \mathbf{v}_1 negative when a shell is collapsing (i.e. after turnaround). The peculiar velocity along the line of sight to the background QSO will be $\mathbf{v}_{pec} = -R_{\parallel} \cdot (H - \mathbf{v}_1/R_1)$, where $R_{\parallel} = (R_1^2 - R_{\perp}^2)^{1/2}$ and R_{\perp} is the impact parameter.